CRYSTAL GROWTH & DESIGN

pubs.acs.org/crystal

Article

On the Mechanism of Cocrystal Mechanochemical Reaction via Low Melting Eutectic: A Time-Resolved In Situ Monitoring Investigation

Published as part of a Crystal Growth and Design virtual special issue on Emerging Investigators 2022

Paolo P. Mazzeo,* Michele Prencipe, Torvid Feiler, Franziska Emmerling, and Alessia Bacchi

Cite This: *Cryst. Growth Des.* 2022, 22, 4260−4267

Read Online

ACCESS | Metrics & More | Article Recommendations | Supporting Information

ABSTRACT: Mechanochemistry has become a sustainable and attractive cost-effective synthetic technique, largely used within the frame of crystal engineering. Cocrystals, namely, crystalline compounds made of different chemical entities within the same crystal structure, are typically synthesized in bulk via mechanochemistry; however, whereas the macroscopic aspects of grinding are becoming clear, the fundamental principles that underlie mechanochemical cocrystallization at the microscopic level remain poorly understood. Time-resolved in situ (TRIS) monitoring approaches have opened the door to exceptional detail regarding mechanochemical reactions. We here report a clear example of cocrystallization between two solid coformers that proceeds through the formation of a metastable low melting binary eutectic phase. The overall cocrystallization process has been monitored by time-resolved in situ (TRIS) synchrotron X-ray powder diffraction with a customized ball milling setup, currently available at μSpot beamline at BESSY-II, Helmholtz-Zentrum Berlin. The binary system and the low melting eutectic phase were further characterized via DSC, HSM, and VT-XRPD.

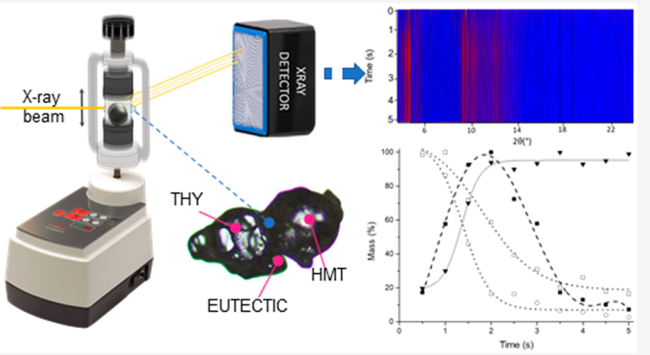

INTRODUCTION

Mechanochemistry has become popular as a sustainable and cost-effective synthetic technique[1−4] for the synthesis of different classes of organic[5,6] and inorganic[7−10] compounds as well as metal−organic materials.[11−17] It is increasingly clear that many traditional solution-based chemical reactions can, in principle, be carried out via mechanochemistry with no (or minimal) use of solvent[1,17−21] and, for this reason, the International Union for Pure and Applied Chemistry (IUPAC) named it as one of ten chemical innovations that would change our world.[22]

Cocrystals are crystalline compounds made of different molecular entities taken together by intermolecular forces within the same crystal structure.[23−27] Cocrystallization has been largely investigated in the modern literature[28−33] since the novel intermolecular networks established between the molecular species involved can tune the physical characteristics[24,34,35] (e.g., solubility, volatility, melting point) of the single molecular entities when in their pure form. A direct correlation of crystal structure/properties is at the basis of the cocrystal design and application of molecular materials.[15,36,37]

Cocrystals are typically synthesized in bulk via mechanochemistry;[18,38−41] however, whereas the macroscopic aspects of grinding are becoming clear, the fundamental principles that underlie mechanochemical cocrystallization at the microscopic level remain poorly understood.[42] Despite their evident utility, this lack of comprehension *de facto* inhibits the outbreak of cocrystals that remain confined within the boundaries of the pharmaceutical industry,[43−46] with the exception of a few examples.[32,39,47−51]

Clearly, the mass transport and reagent diffusion represent the key step of the overall cocrystal formation process. Only a few interpretations reported in the recent literature suggest that the diffusion process can occur through a gas,[52,53] liquid,[42,54,55] or amorphous[56] phase as a function of the coformers used.

Time-resolved in situ (TRIS) monitoring approaches have opened the door to exceptional detail regarding mechanochemical reactions.[57−60]

We here report direct evidence of solid−solid cocrystal formation between thymol (an essential oil component extracted from the thyme plants) and hexamethylenetetramine (HMT) that proceeds through the formation of a metastable binary low-melting eutectic (LME) (Scheme 1).

Received: March 1, 2022
Revised: May 17, 2022
Published: June 1, 2022

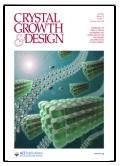

Scheme 1. Schematic Representation of the THY:HMT 3:1 Cocrystals[a]

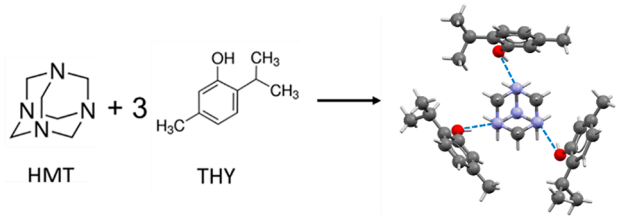

[a]Thumbnail image of the corresponding crystalline structures showing the coformers assemblies. All non-H atoms are reported in ball-and-stick style. Color code: C = gray, N = blue, O = red. Hydrogen atoms are reported in capped stick style for the sake of clarity. Blue dashed lines represent the intermolecular H-bonds.

LME is a binary phase composition whose melting point lies below ambient temperature. The formation of a liquid intermediate has a key role in the mass transport of the coformers in solventless cocrystal formation.

The whole mechanochemical process has been monitored by fast time-resolved in situ (TRIS) synchrotron radiation X-ray powder diffraction (XRPD)[57−59,61,62] at a subsecond data collection frequency, and the low-melting eutectic has been fully characterized by thermal analyses (DSC, HSM, VT-XRPD).

The present cocrystal THY:HMT 3:1 has already been proposed elsewhere within the frame of green pesticides[50] and food preservative alternatives[51] with the thymol biologically active against Gram− and Gram+ pathogens.[50,51,63,64]

However, the low water solubility and high volatility of pure thymol intrinsically limit its direct application in the agrochemical and food industry. Cocrystallization has been recently proposed to mitigate its negative performances, thus obtaining a stimuli-responsive material able to tune the release of the essential oils components as a function of the environmental conditions.[50]

EXPERIMENTAL SECTION

Fast Time-Resolved In Situ Monitoring. The ball mill grinding experiments were performed by means of a Fritsch Pulverisette 23 shaker mill with a vertical movement. This mill has a fixed amplitude of 9 mm and adjustable frequency from 15 to 50 Hz with an adjustable timer. A 2.3 mL jar was custom-designed at BAM and consists of three pieces, two stainless steel or polyvinyl chloride (PVC) end pieces and a transparent Perspex middle segment of 0.75 mm thickness. The overall size of the jar is 40 mm with an internal diameter of 12 mm.[60] X-ray powder diffraction (XRPD) data were collected at μSpot (BESSY-II, Helmholtz Zentrum Berlin) with a low-energy incident beam (17 KeV) of ø 150 μm and an Eiger 9 M 2D detector. Data were collected with an accumulation time of 500 ms per frame while the mill was shaking. Sample-to-detector distance was set at ca. 250 mm. Sequential multiphase Rietveld refinement was performed with TOPAS v 6[65] to extrapolate the relative amount of the chemical species involved in the mechanochemical reaction.

Hot Stage Microscopy (HSM). Cocrystallization of THY and HMT was monitored placing a few crystals (μm order of magnitude) of the two coformers on a glass slide and brought them into contact with a spatula. Different firing profiles (heating and cooling) have been performed by means of a Linkam LTS420 hot stage. The first heating profile was performed by increasing the temperature from 10 to 30 °C at 1 °C min^{-1}. The sample was then cooled at 5 °C min^{-1} down to 10 °C and then heated again at 40 °C. The whole process was recorded by means of an Euromex 18MP camera placed on a trinocular optic microscope equipped with a 100× magnification lens.

Variable Temperature X-ray Powder Diffraction (VT-XRPD). VT-XRPD measurements of the THY:HMT 3:1 cocrystal were carried out in parallel beam geometry with CuKα radiation on a Rigaku Smartlab XE diffractometer equipped with an Anton-Paar TTK600 nonambient chamber with flat copper sample holder. Data were collected in Bragg−Brentano geometry with the radiation source fix at $\omega = 4°$ and the Hypix3000 2D solid-state detector at $2\theta = 13°$. The solid-state detector was used in 2D mode and still images were collected with an accumulation time of 3 s. Data collection was performed at ambient pressure heating the sample from 20 to 60 °C at 5 °C min^{-1}, then cooling it to 10 °C at 5 °C min^{-1} and heating again to 60 °C at 5 °C min^{-1}. At the end of the firing profile, the melt sample was slowly thermalized to ambient conditions. Powder patterns were extrapolated integrating the resulting 2D images in the range of $163° < \beta < 197°$ to obtain the powder pattern in the range of 5−19° 2θ. Results are reported in Supporting Information Figures 19−24.

Thermal Analyses. Binary mixtures of THY and HMT were mechanochemically prepared by grinding the coformers at different molar fractions for 30 min at 500 rpm in a Retsch 100 PM planetary ball mill. A 12 mL steel jar was loaded with ca. 300 mg of each mixture and two 9 mm steel ball bearings. Differential scanning calorimetry (DSC) analysis was performed with a PerkinElmer Diamond equipped with a ULSP 90 ultracooler. Thermal analyses were carried out in closed 10 μL Al-pans. All mixtures with $\chi_{HMT} < 0.33$ were exposed to a 20 °C/100 °C/−20 °C/100 °C heating−cooling−heating firing profile. For the mixtures with $\chi_{HMT} \geq 0.33$, thus with an excess of HMT with respect to the 3:1 cocrystal, a single heating ramp from 20 to 300 °C was performed due to the decomposition process of HMT. All measurements were performed at 5 °C min^{-1} at atmospheric pressure under a constant flow of nitrogen (20 μL min^{-1}). The enthalpy of the endothermic or exothermic events, reported in J g^{-1}, were determined by integrating the area underneath the thermal peaks.

Binary Phase Diagram. THY:HMT binary mixtures at different molar ratios were tested to extrapolate the solid/liquid equilibrium curves for THY:HMT 3:1 cocrystal and the single coformers. The thymol liquidus curve was experimentally calculated according to the Schröder−Laar equation,[66] while the cocrystal liquidus curve was obtained by fitting the experimental data with a second-order polynomial function (see SI for details). Due to the HMT decomposition, the liquidus curve of the HMT could only be approximated.

RESULTS AND DISCUSSION

Synthesis. The THY:HMT 3:1 cocrystal has been synthesized by grinding the two coformers together in the stoichiometric ratio (THY = 154 mg, HMT = 450 mg). As soon as the two solids were gently bent together, a low melting eutectic formed that became dominant after a few minutes of blending. By grinding the so-formed sticky paste for about 30 min, a whitish solid was obtained. The titled compound was alternatively synthesized by grinding the two coformers in the appropriate stoichiometry in a Retsch 100 PM planetary ball mill for 30 min at 500 rpm. A 12 mL steel jar was loaded with ca. 300 mg and two 9 mm steel ball bearings.

The crystal structure of the cocrystal already reported by Mazzeo et al.[50] consists of supramolecular HMT:THY_3 aggregates that crystallize in the $P\bar{1}$ space group with a very high molecular multiplicity ($Z' = 4$, $Z'' = 16$). Each independent HMT is hydrogen bonded to three THY molecules in a pseudotrigonal arrangement, thus forming columns of the HMT:THY_3 aggregates that run along the *a*-axis (Figure 1).

Time-Resolved In Situ (TRIS) Monitoring. The cocrystal synthesis was monitored via TRIS-XRPD with the milling setup recently presented by Lampronti et al.[60] A Perspex jar

https://doi.org/10.1021/acs.cgd.2c00262
Cryst. Growth Des. 2022, 22, 4260−4267

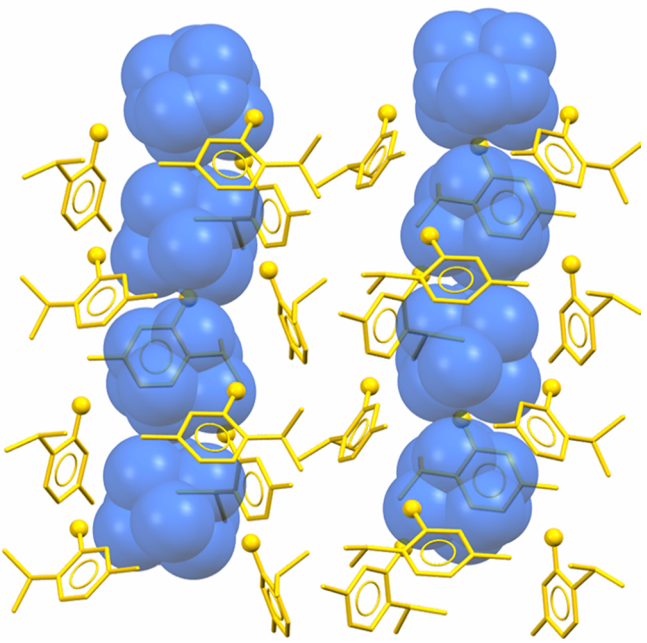

Figure 1. Arrays of THY trimers arranged in columns running along the *a*-axis. HMT is reported in the blue spacefill style, while thymol is shown in the yellow capped stick style. Oxygen atoms in thymol molecules are highlighted in the ball-and-stick style. Hydrogen atoms are removed for the sake of clarity.

with 0.75 mm wall thickness has been loaded with 0.5 mmol of THY and 1.5 mmol of HMT and one 7 mm steel ball bearing (Figure 2). As reported in the Experimental Section, the milling equipment is placed in the synchrotron hutch with the beam passing through the jar. Ideally, the diffraction occurs from a single point, but with the geometry proposed, the beam passes through an elongated sample volume, thereby resulting in a broadening, and ultimately splitting, of the diffracted peaks. XRPD data were collected every 500 ms, while the jar was shaken at 50 Hz. The total conversion occurs in less than 5 s after which only the cocrystal is present. As the coformers are very prone to react at ambient conditions by forming the low melting eutectic binary phase, the jar was loaded at the very last; however, some traces of cocrystal are already present after the first XRPD pattern (Figure 3).

During the milling experiment, it has been demonstrated that part of the milled powder adheres to the jar wall while the remaining powder flows within the jar. This gives rise to the splitting of each measured diffraction peaks into three main components. The inner and outer scattering components arise from powder adhered to the front and back walls of the milling jar, respectively (see $\vec{s_1}$ and $\vec{s_3}$ in Figure 2), while the scattered intensity between these extremes (see $\vec{s_2}$ in Figure 2) arises from powder which flows freely within the jar. The triplet peak shape (Figure 2) was described with three bell-shaped functions: two split-modified Thompson-Cox-Hastings pseudo-Voigt functions for $\vec{s_1}$ and $\vec{s_3}$, plus one Gaussian function for $\vec{s_2}$. The peak displacement caused by each of the scattering vectors $\vec{s_1}$, $\vec{s_2}$, and $\vec{s_3}$, was corrected by modeling the peak positions as reported in Lampronti et al.[60]

A multiphase Rietveld Refinement was performed on the XRPD patterns considering the crystalline phase of each

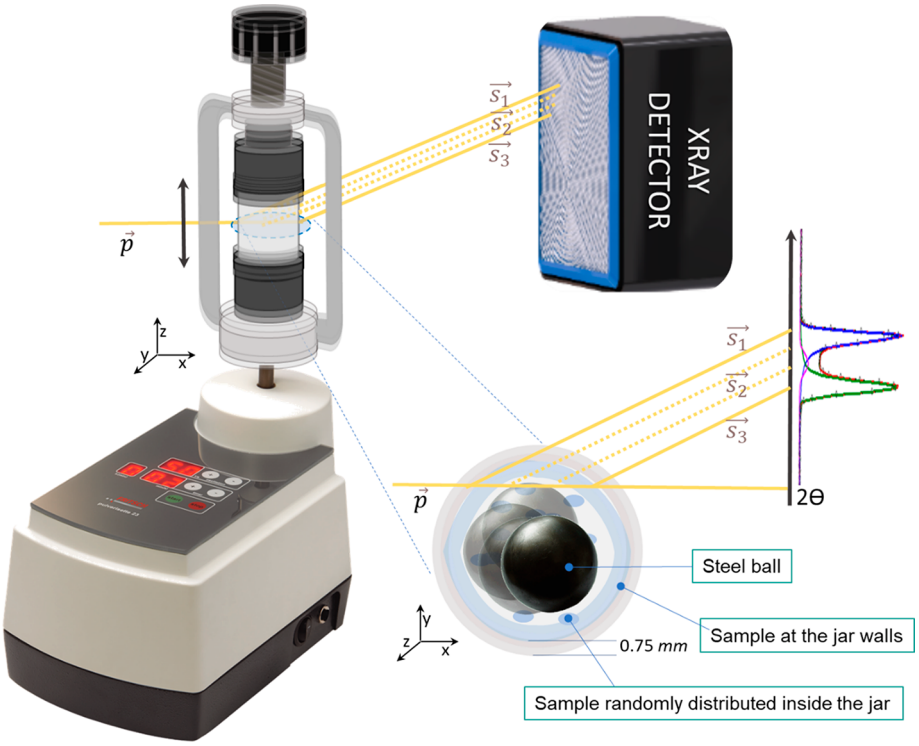

Figure 2. Schematic representation of the milling setup used in this study. The PMMA jars are used with the Fritsch *P*23. The primary X-ray beam $\vec{p}$ (yellow line) passes through the jar and is diffracted by the sample contained within (light blue). Diffraction with this setup results in splitting of each Bragg reflection into a convolution of 2θ positions as the powder inside the jar is distributed across different locations and hence a range of sample-to-detector distances.

https://doi.org/10.1021/acs.cgd.2c00262
Cryst. Growth Des. 2022, 22, 4260−4267

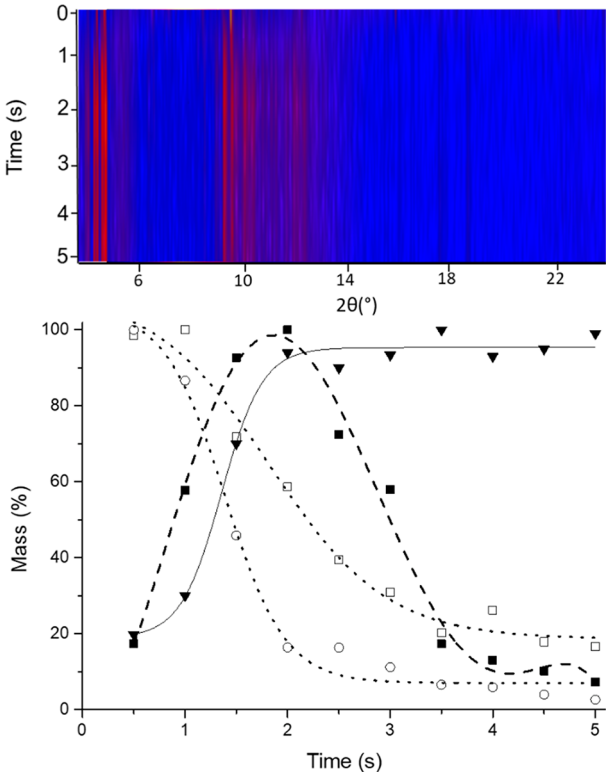

Figure 3. (top) Heatmap plot of XRPD patterns collected as a function of milling time. (bottom) Semiquantitative phase analysis (sQPA) performed via Rietveld Refinement: Experimental data for cocrystal (▼), eutectic phase (■), THY (□), and HMT (○) reported as mass % normalized respect to the maxima of each chemical species. Sigmoidal fit of cocrystal data (solid black line), polynomial fit of the eutectic metastable phase (dashed black line), and sigmoidal fit of coformers (dotted, black line) as a function of the milling time.

coformer, the cocrystal, and the amorphous phase of the intermediate LME which contributes to the background.

To deconvolute the intrinsic amorphous contribution to the massive extrinsic background due to the Perspex jar, the XRPD pattern of the empty jar was collected in the same experimental conditions and included in the Rietveld Refinement input (see SI for further details).

As reported in Figure 3, the intensity of the single coformer phases monotonically decrease as a function of the milling time. The eutectic phase grew as a metastable intermediate thus increasing in the first part of the milling process and then decreasing to leave the stage to the cocrystal after 5 s from the beginning of the milling process.

Low Melting Eutectic Characterization. The binary phase diagram confirms that the amorphous quality observed when the two coformers come into contact is indeed the eutectic phase, which is characterized by a melting point below the ambient temperature.

The liquidus curve of THY was obtained using the Schröder−Laar equation[66] (eq 1) where χ_{THY} is the experimental molar ratio of THY in the mixture under investigation and T_{THY} is the melting temperature of thymol as pure component.

Due to the limited number of experimentally accessible data in the narrow range of molar ratio, the cocrystal liquidus curve was obtained with a second-order polynomial fit (eq 2). See SI for further details.

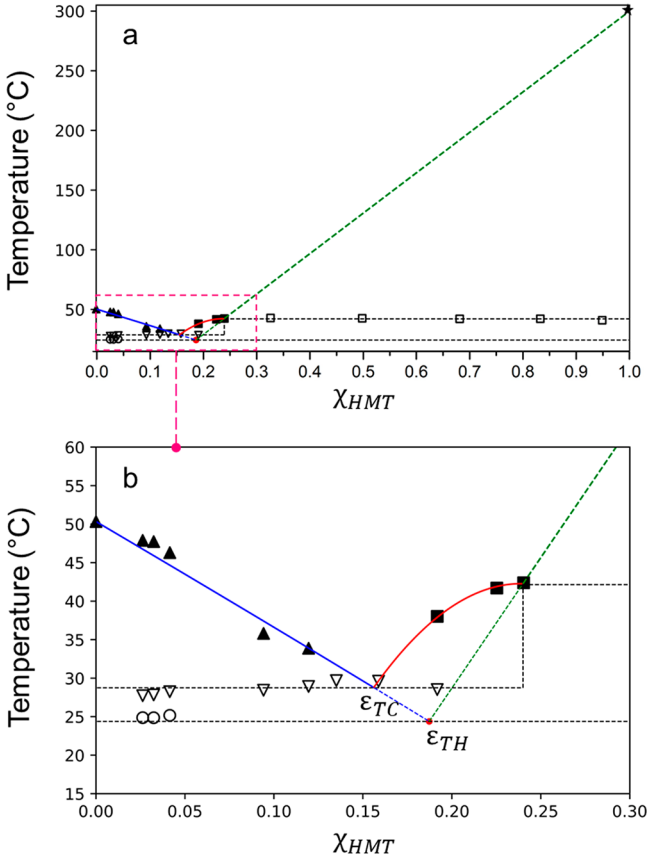

Figure 4. a. Binary solid−liquid phase diagram for the THY/HMT system. Solid lines represent the *liquidus* curves; dashed black lines represent the *solidus* curves. THY, HMT, and cocrystal liquidus curves are depicted in blue, green, and red, respectively. b. Magnified portion of the binary phase in the range of $0 < \chi_{HMT} < 0.30$ and 15 °C < T < 60 °C. The liquidus curves intersect each other at the eutectic composition ε_{TC} (χ_{HMT} = 0.156, T_m = 28.75 °C) and ε_{TH} (χ_{HMT} = 0.187, T = 24.8 °C). Experimental melting points are reported as follows: ▲ = T_{melt} of THY residue; ■ = T_{melt} of cocrystal residue; ★ = $T_{decomposition}$ of HMT; ▽ = T_{melt} of ε_{TC}; ○ = T_{melt} of ε_{TH}.

$$\ln \chi_{THY} = \frac{\Delta H^{\circ}_{THY}}{R}\left(\frac{1}{T_{THY}} - \frac{1}{T_{calc}}\right) \quad (1)$$

$$T_{calc} = a(\chi_{HMT})^2 + b(\chi_{HMT}) + c \quad (2)$$

The liquidus curve of HMT was not experimentally derived due to its endothermic decomposition which prevented the accurate evaluation of the melting point of binary mixtures with an excess of HMT ($\chi_{HMT} > 0.33$). A linear fit passing through the pure HMT melting/decomposition and the cocrystal melting represent a first-order approximation of the liquidus curve of HMT. The liquidus curves of THY and HMT intersect at the metastable eutectic compositions ε_{TH}, which is characterized by a melting point below ambient temperature in the standard laboratory conditions ($T\varepsilon_{TH}$ = 24.38 °C) (Figure 4).

As a further proof, the thermal analyses performed on binary mixture with a large excess of THY ($\chi_{HMT} < 0.04$) showed an indented exothermic peak in the cooling run that can be attributed to the concomitant crystallization of the single coformers. The binary eutectic phase thus clearly melts at 24.86 °C in the second heating run as reported in Figure 5, which is consistent with the temperature extrapolated from the

https://doi.org/10.1021/acs.cgd.2c00262
Cryst. Growth Des. 2022, 22, 4260−4267

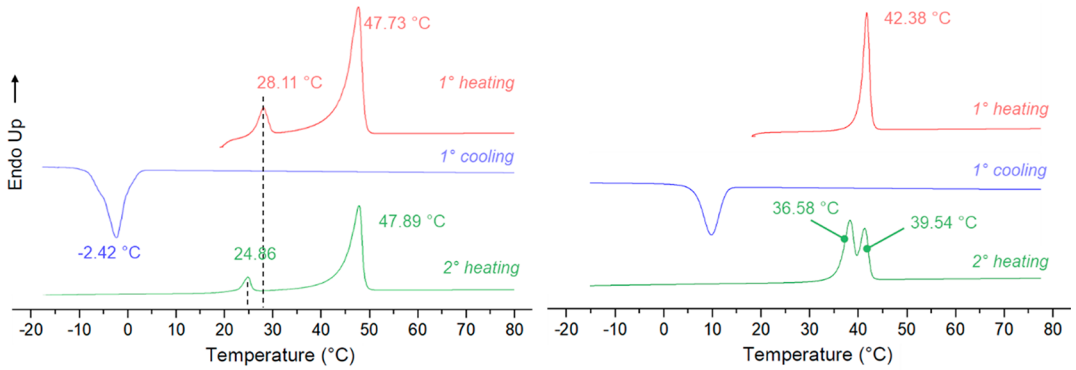

Figure 5. Differential scanning calorimetry traces (endo- up) collected on a binary mixture with χ_{HMT} = 0.026 (a) and χ_{HMT} = 0.240 (b) composition. The firing profile consists of the first heating run from 20 to 80 °C (red line), a cooling run from 80 to −20 °C (blue line) followed by a second heating run from −20 to 80 °C (green line).

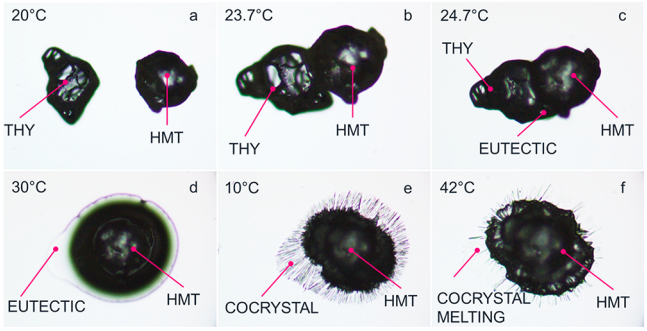

Figure 6. Solid-state reaction between THY and HMT as a function of temperature monitored by HSM. (Mag. 100×) (a) coformers are placed at 20 °C on the glass slide. The crystalline species are solid. (b,c) the THY-HMT eutectic composition starts melting at 23.7 °C. (d) The eutectic is completely melted at 30 °C. A solid residue of coformer is still present. (e) THY:HMT cocrystal crystallized from the eutectic at 10 °C during the cooling process. (f) Cocrystal melts as expected at 42 °C.

binary phase diagram. In Figure 4, the experimental melting point of the LME binary eutectic composition are reported as hole circles.

The *liquidus* curve of THY also intersects the *liquidus* of cocrystal at the eutectic composition ε_{TC} (χ_{HMT} = 0.156, T_m = 28.73 °C) evidenced by hole triangles in Figure 4. All DSC traces are individually reported in SI.

The formation of the LME phase as intermediate in the cocrystal formation was additionally described by HSM. A few crystals of THY and HMT (μm order of magnitude) were placed on a glass slide at 10 °C. The temperature was then raised up to 30 °C at 1 °C min^{-1}; thus a massive melting of the LME was observed along with a solid residue of the coformers. The sample was then cooled to 10 °C, and a clear crystallization process occurs (Figure 6).

The thermal analysis performed on the cocrystal (χ_{HMT} = 0.25) surprisingly showed in DSC an endothermic event in the second heating of the firing profile at a lower temperature with respect to the first heating run. The thermogram reported in Figure 5 (right, green line) shows two maxima which should be

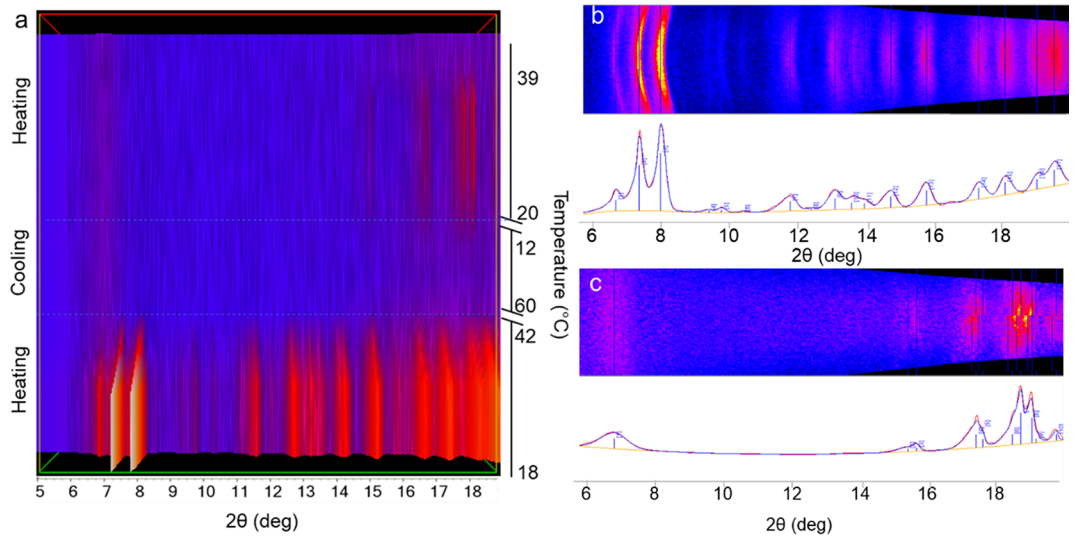

Figure 7. a. Heatmap plot of XRPD patterns extrapolated by integrating the 2D images collected during the VT-XRPD measurement correlated with the acquisition temperature. For the sake of clarity, the temperature scale is not entirely reported, and only relevant events are displayed. b. 2D-XPRD pattern collected at 19.2 °C during the first heating run of the firing profile and its integrated 1D-XRPD pattern corresponding to THY:HMT cocrystal. c. 2D-XPRD pattern collected at 24 °C during the second heating run of the firing profile and its integrated 1D-XRPD pattern corresponding to THY-HMT kinetic phase.

https://doi.org/10.1021/acs.cgd.2c00262
Cryst. Growth Des. 2022, 22, 4260−4267

better described as a multistep thermal event consisting of two concomitant endothermic and exothermic processes.

A TRIS-VT-XRPD experiment was then performed to clarify the nature of these thermal events. The THY:HMT 3:1 cocrystal was placed into a nonambient chamber mounted on a laboratory diffractometer (see Experimental Section). 2D data were collected every 3 s, while the sample was heated/cooled in the same firing profile conditions used in the DSC analysis. The cocrystal was the only phase present at the beginning of the firing profile which melted at ca. 42 °C. During the cooling run, a new phase appeared at 12 °C and remained stable during the heating run up to 39 °C when it melted (Figure 7). After melting, the heating was turned off and the sample slowly thermalized to ambient temperature. Single crystals suitable for SCXRD were obtained that confirm the recrystallization of the native THY:HMT cocrystal.

This suggests that the thermal profile influences the formation of a metastable phase that can only be isolated by a kinetically controlled cooling ramp.

CONCLUSIONS

The cocrystallization of thymol and hexamethylenetetramine occurs via solvent-free mechanochemical reaction and proceeds through the formation of a metastable low melting eutectic phase that plays a key role in the mass transport of the coformers. The whole process was monitored via time-resolved in situ X-ray powder diffraction with a customized ball milling setup, currently available at the μSpot beamline at the BESSY-II synchrotron facility. The two coformers react as soon as they are blended, thus forming a low-melting eutectic phase. In the experimental XRPD patterns collected every 500 ms, the intensities of the coformers monotonically decrease, while the background increases as a symptom of the growth of the liquid phase. From the metastable eutectic binary composition, the cocrystallization occurs in less than 5 s. The binary phase diagram suggests that the metastable eutectic phase is indeed characterized by a melting point below ambient temperature, which was further confirmed by hot stage microscopy. A new kinetic phase was observed and isolated through VT-XRPD performed on the binary composition with χ_{HMT} = 0.25, corresponding to the 3:1 THY:HMT stoichiometry.

ASSOCIATED CONTENT

Supporting Information

The Supporting Information is available free of charge at https://pubs.acs.org/doi/10.1021/acs.cgd.2c00262.

Differential scanning calorimetry diagrams, VT-XRPD 2D patterns, Rietveld refinement details (PDF)

AUTHOR INFORMATION

Corresponding Author

Paolo P. Mazzeo − *Department of Chemistry, Life Sciences and Environmental Sustainability, University of Parma, 43124 Parma, Italy; Biopharmanet-TEC, University of Parma, 43124 Parma, Italy;* orcid.org/0000-0002-5787-3609; Email: paolopio.mazzeo@unipr.it

Authors

Michele Prencipe − *Department of Chemistry, Life Sciences and Environmental Sustainability, University of Parma, 43124 Parma, Italy*

Torvid Feiler − *BAM Federal Institute for Materials Research and Testing, D-12489 Berlin, Germany*

Franziska Emmerling − *BAM Federal Institute for Materials Research and Testing, D-12489 Berlin, Germany;* orcid.org/0000-0001-8528-0301

Alessia Bacchi − *Department of Chemistry, Life Sciences and Environmental Sustainability, University of Parma, 43124 Parma, Italy; Biopharmanet-TEC, University of Parma, 43124 Parma, Italy;* orcid.org/0000-0001-5675-9372

Complete contact information is available at: https://pubs.acs.org/10.1021/acs.cgd.2c00262

Author Contributions

The manuscript was written through contributions of all authors. All authors have given approval to the final version of the manuscript.

Notes

The authors declare no competing financial interest.

ACKNOWLEDGMENTS

This work has benefited from the equipment and framework of the COMP-HUB Initiative, funded by the "Departments of Excellence" program of the Italian Ministry for Education, University and Research (MIUR, 2018−2022). COST Action CA18112 - Mechanochemistry for Sustainable Industry is acknowledged.

ABBREVIATIONS

THY, Thymol; HMT, Hexamethylenetetramine; THY:HMT, Thymol: Hexamethylenetetramine 3:1 cocrystal; LME, Low Melting Eutectic; TRIS, Time-Resolved In Situ

REFERENCES

(1) Howard, J. L.; Cao, Q.; Browne, D. L. Mechanochemistry as an Emerging Tool for Molecular Synthesis: What Can It Offer? *Chem. Sci.* **2018**, *9*, 3080−3094.

(2) James, S. L.; Friščić, T. Mechanochemistry. *Chem. Soc. Rev.* **2013**, *42*, 7494−7496.

(3) James, S. L.; Adams, C. J.; Bolm, C.; Braga, D.; Collier, P.; Friščić, T.; Grepioni, F.; Harris, K. D. M.; Hyett, G.; Jones, W.; Krebs, A.; Mack, J.; Maini, L.; Orpen, A. G.; Parkin, I. P.; Shearouse, W. C.; Steed, J. W.; Waddell, D. C. Mechanochemistry: Opportunities for New and Cleaner Synthesis. *Chem. Soc. Rev.* **2012**, *41*, 413−447.

(4) Tan, D.; García, F. Main Group Mechanochemistry: From Curiosity to Established Protocols. *Chem. Soc. Rev.* **2019**, *48*, 2274−2292.

(5) Margetić, D.; Štrukil, V. Recent Advances in Mechanochemical Organic Synthesis. In *Organic Synthesis*, Nandeshwarappa, B. P., Ed.; IntechOpen, 2020.

(6) Kulla, H.; Haferkamp, S.; Akhmetova, I.; Röllig, M.; Maierhofer, C.; Rademann, K.; Emmerling, F. In Situ Investigations of Mechanochemical One-Pot Syntheses. *Angew. Chemie Int. Ed.* **2018**, *57* (20), 5930−5933.

(7) Brekalo, I.; Yuan, W.; Mottillo, C.; Lu, Y.; Zhang, Y.; Casaban, J.; Holman, K. T.; James, S. L.; Duarte, F.; Williams, P. A.; Harris, K. D. M.; Friščić, T. Manometric Real-Time Studies of the Mechanochemical Synthesis of Zeolitic Imidazolate Frameworks. *Chem. Sci.* **2020**, *11* (8), 2141−2147.

(8) Belenguer, A. M.; Lampronti, G. I.; De Mitri, N.; Driver, M.; Hunter, C. A.; Sanders, J. K. M. Understanding the Influence of Surface Solvation and Structure on Polymorph Stability: A Combined Mechanochemical and Theoretical Approach. *J. Am. Chem. Soc.* **2018**, *140* (49), 17051−17059.

(9) Katsenis, A. D.; Puškarić, A.; Štrukil, V.; Mottillo, C.; Julien, P. A.; Užarević, K.; Pham, M. H.; Do, T. O.; Kimber, S. A. J.; Lazić, P.;

Magdysyuk, O.; Dinnebier, R. E.; Halasz, I.; Friščić, T. In Situ X-Ray Diffraction Monitoring of a Mechanochemical Reaction Reveals a Unique Topology Metal-Organic Framework. *Nat. Commun.* **2015**, *6* (1), 1−8.
(10) Gazzurelli, C.; Carcelli, M.; Mazzeo, P. P.; Mucchino, C.; Pandolfi, A.; Migliori, A.; Pietarinen, S.; Leonardi, G.; Rogolino, D.; Pelagatti, P. Exploiting the Reducing Properties of Lignin for the Development of an Effective Lignin@Cu2O Pesticide. *Adv. Sustain. Syst.* **2022**, 2200108.
(11) Stolar, T.; Batzdorf, L.; Lukin, S.; Žilić, D.; Motillo, C.; Friščić, T.; Emmerling, F.; Halasz, I.; Užarević, K. In Situ Monitoring of the Mechanosynthesis of the Archetypal Metal-Organic Framework HKUST-1: Effect of Liquid Additives on the Milling Reactivity. *Inorg. Chem.* **2017**, *56* (11), 6599−6608.
(12) Souza, B. E.; Rudić, S.; Titov, K.; Babal, A. S.; Taylor, J. D.; Tan, J. C. Guest-Host Interactions of Nanoconfined Anti-Cancer Drug in Metal-Organic Framework Exposed by Terahertz Dynamics. *Chem. Commun.* **2019**, *55* (27), 3868−3871.
(13) Gazzurelli, C.; Migliori, A.; Mazzeo, P. P.; Carcelli, M.; Pietarinen, S.; Leonardi, G.; Pandolfi, A.; Rogolino, D.; Pelagatti, P. Making Agriculture More Sustainable: An Environmentally Friendly Approach to the Synthesis of Lignin@Cu Pesticides. *ACS Sustain. Chem. Eng.* **2020**, *8*, 14886−14895.
(14) Maini, L.; Mazzeo, P. P.; Farinella, F.; Fattori, V.; Braga, D. Mechanochemical Preparation of Copper Iodide Clusters of Interest for Luminescent Devices. *Faraday Discuss.* **2014**, *170*, 93−107.
(15) Braga, D.; Grepioni, F.; Maini, L.; Mazzeo, P. P.; Ventura, B. Solid-State Reactivity of Copper(i) Iodide: Luminescent 2D-Coordination Polymers of CuI with Saturated Bidentate Nitrogen Bases. *New J. Chem.* **2011**, *35*, 339−344.
(16) Maini, L.; Braga, D.; Mazzeo, P. P.; Maschio, L.; Rérat, M.; Manet, I.; Ventura, B. Dual Luminescence in Solid CuI(Piperazine): Hypothesis of an Emissive 1-D Delocalized Excited State. *Dalt. Trans.* **2015**, *44* (29), 13003−13006.
(17) Gazzurelli, C.; Solzi, M.; Cugini, F.; Pio Mazzeo, P.; Bacchi, A.; Pelagatti, P. Comparison of Different Synthetic Approaches for the Fabrication of a Bio-Inspired 1D-Coordination Polymer: From Solution Chemistry to Mechanochemistry. *Inorg. Chim. Acta* **2022**, *539*, 121010.
(18) Braga, D.; Dichiarante, E.; Grepioni, F.; Lampronti, G. I.; Maini, L.; Mazzeo, P. P.; D'Agostino, S. Mechanical Preparation of Crystalline Materials. An Oxymoron? In *Supramolecular Chemistry*; John Wiley & Sons, Ltd: Chichester, UK, 2012; pp 1−15.
(19) Kaupp, G. Mechanochemistry: The Varied Applications of Mechanical Bond-Breaking. *CrystEngComm* **2009**, *11* (3), 388−403.
(20) Tan, D.; Friščić, T. Mechanochemistry for Organic Chemists: An Update. *Eur. J. Org. Chem.* **2018**, *2018*, 18−33.
(21) Kubota, K.; Pang, Y.; Miura, A.; Ito, H. Redox Reactions of Small Organic Molecules Using Ball Milling and Piezoelectric Materials. *Science (80-.)* **2019**, *366* (6472), 1500−1504.
(22) Gomollón-Bel, F. Ten Chemical Innovations That Will Change Our World: IUPAC Identifies Emerging Technologies in Chemistry with Potential to Make Our Planet More Sustainable. *Chem. Int.* **2019**, *41* (2), 12−17.
(23) Aakeröy, C. B.; Salmon, D. J. Building Co-Crystals with Molecular Sense and Supramolecular Sensibility. *CrystEngComm* **2005**, *7* (72), 439−448.
(24) Bhattacharya, S.; Peraka, K. S.; Zaworotko, M. J. The Role of Hydrogen Bonding in Co-Crystals. In *Co-crystals: Preparation, Characterization and Applications*; Royal Society of Chemistry, 2018; pp 33−79.
(25) Mazzeo, P. P.; Canossa, S.; Carraro, C.; Pelagatti, P.; Bacchi, A. Systematic Coformer Contribution to Cocrystal Stabilization: Energy and Packing Trends. *CrystEngComm* **2020**, *22*, 7341−7349.
(26) Braga, D.; Grepioni, F.; Maini, L. The Growing World of Crystal Forms. *Chem. Commun.* **2010**, *46* (34), 6232−6242.
(27) Aakeröy, C. B.; Sinha, A. S. *Co-Crystals*; Monographs in Supramolecular Chemistry; The Royal Society of Chemistry, 2018.
(28) Bacchi, A.; Mazzeo, P. P. Cocrystallization as a Tool to Stabilize Liquid Active Ingredients. *Crystallogr. Rev.* **2021**, *27* (2), 102−123.
(29) Aakeroy, C. Is There Any Point in Making Co-Crystals? *Acta Crystallogr. Sect. B Struct. Sci. Cryst. Eng. Mater.* **2015**, *71*, 387−391.
(30) Gavezzotti, A.; Colombo, V.; Lo Presti, L. Facts and Factors in the Formation and Stability of Binary Crystals. *Cryst. Growth Des.* **2016**, *16*, 6095−6104.
(31) Zukerman-Schpector, J.; Tiekink, E. R. T. What Is a Co-Crystal? *Zeitschrift für Krist.* **2008**, *223* (3), 233−234.
(32) Mazzeo, P. P.; Carraro, C.; Arns, A.; Pelagatti, P.; Bacchi, A. Diversity through Similarity: A World of Polymorphs, Solid Solutions, and Cocrystals in a Vial of 4,4′-Diazopyridine. *Cryst. Growth Des.* **2020**, *20* (2), 636−644.
(33) Fornari, F.; Montisci, F.; Bianchi, F.; Cocchi, M.; Carraro, C.; Cavaliere, F.; Cozzini, P.; Peccati, F.; Mazzeo, P. P.; Riboni, N.; Careri, M.; Bacchi, A. Chemometric-Assisted Cocrystallization: Supervised Pattern Recognition for Predicting the Formation of New Functional Cocrystals. *Chemom. Intell. Lab. Syst.* **2022**, *226*, 104580.
(34) Fischer, F.; Heidrich, A.; Greiser, S.; Benemann, S.; Rademann, K.; Emmerling, F. Polymorphism of Mechanochemically Synthesized Cocrystals: A Case Study. *Cryst. Growth Des.* **2016**, *16* (3), 1701−1707.
(35) Cable, M. L.; Vu, T. H.; Malaska, M. J.; Maynard-Casely, H. E.; Choukroun, M.; Hodyss, R. A Co-Crystal between Acetylene and Butane: A Potentially Ubiquitous Molecular Mineral on Titan. *ACS Earth Sp. Chem.* **2019**, *3* (12), 2808−2815.
(36) Lee, T.; Chen, H. R.; Lin, H. Y.; Lee, H. L. Continuous Co-Crystallization As a Separation Technology: The Study of 1:2 Co-Crystals of Phenazine−Vanillin. *Cryst. Growth Des.* **2012**, *12* (12), 5897−5907.
(37) Trivedi, D. R.; Fujiki, Y.; Fujita, N.; Shinkai, S.; Sada, K. Crystal Engineering Approach To Design Colorimetric Indicator Array To Discriminate Positional Isomers of Aromatic Organic Molecules. *Chem. - An Asian J.* **2009**, *4* (2), 254−261.
(38) Braga, D.; Maini, L.; Grepioni, F. Mechanochemical Preparation of Co-Crystals. *Chem. Soc. Rev.* **2013**, *42* (18), 7638−7648.
(39) Mazzeo, P. P.; Pioli, M.; Montisci, F.; Bacchi, A.; Pelagatti, P. Mechanochemical Preparation of Dipyridyl-Naphthalenediimide Cocrystals: Relative Role of Halogen-Bond and $\pi-\pi$ Interactions. *Cryst. Growth Des.* **2021**, *21*, 5687.
(40) Braga, D.; Grepioni, F.; Maini, L.; Mazzeo, P. P.; Rubini, K. Solvent-Free Preparation of Co-Crystals of Phenazine and Acridine with Vanillin. *Thermochim. Acta* **2010**, *507−508*, 1−8.
(41) Braga, D.; Maini, L.; Mazzeo, P. P.; Ventura, B. Reversible Interconversion between Luminescent Isomeric Metal-Organic Frameworks of [Cu4I4(DABCO)2] (DABCO = 1,4-Diazabicyclo[2.2.2]Octane). *Chem. - A Eur. J.* **2010**, *16* (5), 1553−1559.
(42) Chadwick, K.; Davey, R.; Cross, W. How Does Grinding Produce Co-Crystals? Insights from the Case of Benzophenone and Diphenylamine. *CrystEngComm* **2007**, *9* (9), 732−734.
(43) Trask, A. V. An Overview of Pharmaceutical Cocrystals as Intellectual Property. *Mol. Pharmaceutics* **2007**, *4* (3), 301−309.
(44) Berry, D. J.; Steed, J. W. Pharmaceutical Cocrystals, Salts and Multicomponent Systems; Intermolecular Interactions and Property Based Design. *Adv. Drug Delivery Rev.* **2017**, *117*, 3−24.
(45) Bolla, G.; Nangia, A. Pharmaceutical Cocrystals: Walking the Talk. *Chem. Commun.* **2016**, *52* (54), 8342−8360.
(46) Steed, J. W. The Role of Co-Crystals in Pharmaceutical Design. *Trends Pharmacol. Sci.* **2013**, *34* (3), 185−193.
(47) Aakeroy, C. B.; Wijethunga, T. K.; Benton, J.; Desper, J. Stabilizing Volatile Liquid Chemicals Using Co-Crystallization. *Chem. Commun.* **2015**, *51*, 2425−2428.
(48) Sinha, A. S.; Rao Khandavilli, U. B.; O'Connor, E. L.; Deadman, B. J.; Maguire, A. R.; Lawrence, S. Novel Co-Crystals of the Nutraceutical Sinapic Acid. *CrystEngComm* **2015**, *17* (26), 4832−4841.

https://doi.org/10.1021/acs.cgd.2c00262
Cryst. Growth Des. 2022, 22, 4260−4267

(49) Capucci, D.; Balestri, D.; Mazzeo, P. P.; Pelagatti, P.; Rubini, K.; Bacchi, A. Liquid Nicotine Tamed in Solid Forms by Cocrystallization. *Cryst. Growth Des.* **2017**, *17* (9), 4958−4964.
(50) Mazzeo, P. P.; Carraro, C.; Monica, A.; Capucci, D.; Pelagatti, P.; Bianchi, F.; Agazzi, S.; Careri, M.; Raio, A.; Carta, M.; Menicucci, F.; Belli, M.; Michelozzi, M.; Bacchi, A. Designing a Palette of Cocrystals Based on Essential Oil Constituents for Agricultural Applications. *ACS Sustain. Chem. Eng.* **2019**, *7* (21), 17929−17940.
(51) Bianchi, F.; Fornari, F.; Riboni, N.; Spadini, C.; Cabassi, C. S.; Iannarelli, M.; Carraro, C.; Mazzeo, P. P.; Bacchi, A.; Orlandini, S.; Furlanetto, S.; Careri, M. Development of Novel Cocrystal-Based Active Food Packaging by a Quality by Design Approach. *Food Chem.* **2021**, *347*, 129051.
(52) Rastogi, R. P.; Bassi, P. S.; Chadha, S. L. Mechanism of the Reaction between Hydrocarbons and Picric Acid in the Solid State. *J. Phys. Chem.* **1963**, *67* (12), 2569−2573.
(53) Rastogi, R. P.; Bassi, P. S.; Chadha, S. L. Kinetics of Reaction between Naphtalene and Picric Acid in the Solid State. *J. Phys. Chem.* **1962**, *66* (12), 2707−2708.
(54) Rothenberg, G.; Downie, A. P.; Raston, C. L.; Scott, J. L. Understanding Solid/Solid Organic Reactions. *J. Am. Chem. Soc.* **2001**, *123* (36), 8701−8708.
(55) Biliškov, N. In Situ Monitoring of a Quasi Solid-State Diffusion-Driven Cocrystallization in the Diphenylamine-Benzophenone System. *Cryst. Growth Des.* **2021**, *21* (3), 1434−1442.
(56) Seefeldt, K.; Miller, J.; Alvarez-Núñez, F.; Rodríguez-Hornedo, N. Crystallization Pathways and Kinetics of Carbamazepine−Nicotinamide Cocrystals from the Amorphous State by In Situ Thermomicroscopy, Spectroscopy, and Calorimetry Studies. *J. Pharm. Sci.* **2007**, *96* (5), 1147−1158.
(57) Friščić, T.; Halasz, I.; Beldon, P. J.; Belenguer, A. M.; Adams, F.; Kimber, S. A. J.; Honkimaki, V.; Dinnebier, R. E. Real-Time and in Situ Monitoring of Mechanochemical Milling Reactions. *Nat. Chem.* **2013**, *5*, 66−73.
(58) Halasz, I.; Puškarić, A.; Kimber, S. A. J.; Beldon, P. J.; Belenguer, A. M.; Adams, F.; Honkimäki, V.; Dinnebier, R. E.; Patel, B.; Jones, W.; Štrukil, V.; Friščić, T. Real-Time In Situ Powder X-Ray Diffraction Monitoring of Mechanochemical Synthesis of Pharmaceutical Cocrystals. *Angew. Chemie Int. Ed.* **2013**, *52* (44), 11538−11541.
(59) Batzdorf, L.; Fischer, F.; Wilke, M.; Wenzel, K.-J.; Emmerling, F. Direct In Situ Investigation of Milling Reactions Using Combined X-Ray Diffraction and Raman Spectroscopy. *Angew. Chemie Int. Ed.* **2015**, *54* (6), 1799−1802.
(60) Lampronti, G. I.; Michalchuk, A. A. L.; Mazzeo, P. P.; Belenguer, A. M.; Sanders, J. K. M.; Bacchi, A.; Emmerling, F. Changing the Game of Time Resolved X-Ray Diffraction on the Mechanochemistry Playground by Downsizing. *Nat. Commun.* **2021**, *12* (1), 1−9.
(61) Michalchuk, A. A. L.; Tumanov, I. A.; Konar, S.; Kimber, S. A. J.; Pulham, C. R.; Boldyreva, E. V. Challenges of Mechanochemistry: Is In Situ Real-Time Quantitative Phase Analysis Always Reliable? A Case Study of Organic Salt Formation. *Adv. Sci.* **2017**, *4* (9), 1700132.
(62) Michalchuk, A. A. L.; Emmerling, F. Time-Resolved In Situ Monitoring of Mechanochemical Reactions. *Angew. Chemie Int. Ed.* **2022**, DOI: 10.1002/anie.202117270.
(63) Burt, S. Essential Oils: Their Antibacterial Properties and Potential Applications in Foods—a Review. *Int. J. Food Microbiol.* **2004**, *94* (3), 223−253.
(64) Imdorf, A.; Bogdanov, S.; Ochoa, R. I.; Calderone, N. W. Use of Essential Oils for the Control of Varroa Jacobsoni Oud. in Honey Bee Colonies. *Apidologie* **1999**, *30* (2−3), 209−228.
(65) Coelho, A. A. TOPAS and TOPAS-Academic: An Optimization Program Integrating Computer Algebra and Crystallographic Objects Written in C++: An. *J. Appl. Crystallogr.* **2018**, *51* (1), 210−218.
(66) Prigogine, I.; Defay, R. *Chemical Thermodynamics*; Longmans, Green & Co.: New York, 1954.

https://doi.org/10.1021/acs.cgd.2c00262
Cryst. Growth Des. 2022, 22, 4260−4267